



Large-area, 1964 land cover classifications of Corona spy satellite imagery for the Caucasus Mountains

Afag Rizayeva^{a,*}, Mihai D. Nita^b, Volker C. Radeloff^a

^a SILVIS Lab, Department of Forest and Wildlife Ecology, University of Wisconsin-Madison, 1630 Linden Drive, Madison, WI 53706, USA

^b Department of Forest Engineering, Faculty of Silviculture and Forest Engineering, Transylvania University of Brasov, 1 Sirul Beethoven, Brasov 500123, Romania

ARTICLE INFO

Edited by Dr. Marie Weiss

Keywords:

Land cover mapping
Corona spy satellites
Google Earth Engine (GEE)
Object-oriented image analysis
VHR panchromatic satellite imagery
Caucasus eco-region
Automation

ABSTRACT

Historical land use strongly influences current landscapes and ecosystems making maps of historical land cover an important reference point. However, the earliest satellite-based land cover maps typically date back to the 1980s only, after 30-m Landsat data became available. Our goal was to develop a methodology to automatically map land cover for large areas using high-resolution panchromatic Corona spy satellite imagery for 1964. Specifically, we a) conducted a comprehensive analysis on the feature selection and parameter setting for large-area classification processes for 2.5-m historical panchromatic Corona imagery for a full suite of land cover classes, b) compared the pixel-based and object-oriented methods of classifying the land cover, and c) examined the benefits of adding a digital elevation model for the pixel-based and object-oriented land cover classifications. We mapped land cover in parts of the Caucasus Mountains (158,000 km²), a study area with great variability in land cover types and illumination conditions. The overall accuracies of our pixel-based and object-oriented land cover maps were $63.0 \pm 5.0\%$ and $67.3 \pm 4.0\%$, respectively, showing that object-oriented classifications performed better for Corona satellite data. Incorporating the digital elevation model improved the overall accuracy to $75.3 \pm 3.0\%$ and $78.7 \pm 2.5\%$, respectively. The digital elevation model was especially useful for differentiating forest and snow-and-ice from lakes in mountainous areas affected by cast shadows. Our results highlight the feasibility of accurately and automatically classifying land cover for large areas based on Corona spy satellite imagery for the 1960s. Such land cover maps predate the earliest 30-m Landsat land cover classifications by two decades, and those from high-resolution satellite imagery by four decades. As such, we demonstrate here that Corona imagery can make important contributions to global change science.

1. Introduction

Current landscape structure is strongly affected by past human activities (Munteanu et al., 2017; Wu et al., 2013) and many vegetation types change slowly over time (Barichivich et al., 2013; White et al., 2009). This means that historical information is valuable when assessing current ecosystem patterns and processes (Foster et al., 2003). Similarly, land cover classifications are essential for environmental science (Altmair and Kany, 2002), because they provide information on the status of both natural ecosystems and human land use (Balzter et al., 2015; Yin et al., 2020; Zhu and Woodcock, 2014). The earliest land cover maps typically only date back to the 1980s when 30-m satellite data became available. However, images captured by American spy satellites during the 1960s and '70s provide an opportunity to obtain land cover data for earlier decades (Saleem et al., 2018; Stratoulas and Kabadayi, 2020).

The earliest high-resolution satellite imagery (< 5 m resolution) dates back to the early 1960s, when the first Corona spy satellites were launched (Peebles, 1997). The Corona satellite missions started a series of US reconnaissance satellites operated by the US Air Force and the US Central Intelligence Agency (CIA) (Altmair and Kany, 2002; Norris, 2007; Peebles, 1997). While designed and launched for military purposes, Corona satellite images also contain valuable information about the environment and archaeology (Beck et al., 2007; Casana et al., 2012; Conesa et al., 2015). For example, Corona images can reveal historical urban development patterns (Fekete, 2020; Kennedy, 1998; Lasaponara et al., 2018), lithological structures in the Arctic (Lorenz, 2004), and the retreat of glaciers in Nepal (Bolch et al., 2008). Corona data have also been useful in detecting individual wadi trees in Eastern Desert in Egypt (Andersen, 2006), wild mammal species' occurrences, such as the burrows of the bobak marmot (*Marmota bobak*) in the 1960s (Munteanu

* Corresponding author.

E-mail address: rizayeva@wisc.edu (A. Rizayeva).

<https://doi.org/10.1016/j.rse.2022.113343>

Received 1 August 2022; Received in revised form 19 October 2022; Accepted 30 October 2022

Available online 13 November 2022

0034-4257/© 2022 Elsevier Inc. All rights reserved.

et al., 2020). Additionally, Corona has captured long-term dynamics of ant colonies (Klimeczek et al., 2021), and wildlife habitat information, such as recolonization of new growth forests by capercaillie (*Tetrao urogallus*) (Stăncioiu et al., 2021).

Among its many uses, Corona imagery provide especially valuable information on land cover. For example, Corona images capture the reforestation of abandoned agricultural fields (Jabs-Sobocińska et al., 2021), high conservation value forests (Munteanu et al., 2021), widespread logging after the World War II in the Romanian Carpathians (Nita et al., 2018), and 1960s forest cover in parts of the US and Brazil (Song et al., 2015) and Canada (Franklin et al., 2005). The imagery captures forest loss due to agriculture and settlements in Thailand (Kusanagi et al., 2003), Senegal (Tappan et al., 2000), the Ramganga river basin in India (Gurjar and Tare, 2019), and the Tarim river basin in northwestern China (Veroustraete et al., 2011). Corona images have also been used to identify forest loss due to industrial operations in arctic Russia (Rigina, 2003) and eastern China (Zhang et al., 2020), and forest regrowth along the border of Latvia and Russia (Rendenieks et al., 2020). However, most prior studies of Corona imagery analyzed only small study areas, and the question remains how to map land cover accurately for large areas from Corona imagery.

Large-area land cover maps require both efficient georectification of many Corona images and accurate classification algorithms. For the georectification of Corona imagery, the analysis of forests in Romania by Nita et al. (2018) represented a major breakthrough because it provided a new approach to geo-rectify Corona imagery by applying structure-from-motion algorithms (Nita et al., 2018). However, only forest and non-forests were distinguished, and forest patches were hand-digitized (Nita et al., 2018), as was the case for a study based in Canada (Franklin et al., 2005). Successful pixel-based classifications have been conducted based on image texture metrics (Shahtahmassebi et al., 2017; Song et al., 2015, 2021), unsupervised classification (Kusanagi et al., 2003), and two-dimensional convolutional neural networks (Deshpande et al., 2021). Object-oriented classifications of Corona imagery has only been tested twice: to map forest cover in Latvia (Rendenieks et al., 2020), and agricultural and urban expansion in India (Gurjar and Tare, 2019). However, the former examined forest cover only, not a full suite of land cover classes, and the latter applied considerable manual effort to improve classification accuracy. So, given that prior classifications were either for small areas or classified forests-non-forests only, our first question was how to classify a full suite of land cover classes for a large area automatically from Corona imagery?

Object-oriented classifications, also known as object-based image analysis (OBIA) or geographical object-based image analysis (GEOBIA), typically outperform pixel-level classifications of high-resolution imagery (Blaschke et al., 2000) because objects can be classified based on both spectral and spatial characteristics. Since the first commercial high-resolution satellites were launched in the early 2000s, their images have been widely used for land use and land cover mapping (Lackner and Conway, 2008; Li et al., 2019; Moser et al., 2012). However, large-area (100,000 to 1,000,000 km²) land cover mapping with high-resolution imagery remains uncommon (Khare and Ghosh, 2016, but see Robinson et al., 2019 [160,000 km²]), most likely because the imagery is often costly, data volumes are large, and algorithms are computationally intensive. While object-oriented approaches work well for small study areas (Ma et al., 2017), it is less clear how well they perform for large areas in general, and especially for classifications of a full suite of land cover classes for a large area based on Corona imagery. So, our second question is whether the pixel-based or object-oriented classifications performed better for land-area land cover mapping based on Corona imagery?

Another open question when classifying Corona imagery is if including ancillary data, such as a digital surface model improves classification accuracy. Because Corona images are panchromatic and lack the different spectral bands that 21st century high-resolution satellite sensors provide, elevation information may be especially valuable. One

source of elevation information can be the Corona imagery itself, because for many areas the Corona imagery was obtained as stereoscopic that allow extraction of high-resolution historical digital surface models (Altmaier and Kany, 2002; Galiatsatos et al., 2008; Mészáros et al., 2008). However, where Corona data is not fully stereoscopic, such as in our study area, other digital elevation data may improve classification accuracy.

Our main goal was to develop a methodology to map land cover automatically for a large area from panchromatic Corona satellites imagery. Our objectives were to a) conduct a comprehensive analysis on the feature selection and parameter setting for large-area classification processes for 2.5-m historical panchromatic Corona imagery for a full suite of land cover classes; b) compare the pixel-based and object-oriented methods of classifying the land cover; c) examine the benefits of adding a digital elevation model (DEM) for the pixel-based and object-oriented land cover classification. We expected that object-oriented image analysis would outperform pixel-level classifications, and that adding elevation information would improve classification accuracy substantially.

2. Methods

2.1. Study area

We classified 1964 land cover for a 158,000 km² study area that included parts of the Greater and Lesser Caucasus, and territories of southern Russia, Armenia, Azerbaijan, Georgia, and eastern Turkey (Fig. 1). The elevation in the study area ranges from −6 to 5633 m above sea level, peaking at Mount Elbrus. The Caucasus ecoregion is a global biodiversity hotspot (Myers et al., 2000; Zazanashvili and Mallon, 2009) that includes ecosystems ranging from arid and semi-arid to sub-nival and nival zones. Accordingly, the Caucasus ecoregion has highly heterogeneous landscapes with strong environmental gradients and high variability in elevations and land cover, which makes it a challenging place to map land cover, and a good test site for our study goal.

2.2. Data

Our study area was frequently photographed by Corona spy satellites because of its high strategic importance during the Cold War. We selected data from one KH-4A Corona mission number 1011 (October 8, 1964) because it had only sparse cloud cover. The focal length camera was equal to 610 mm. The Petzval f.3/5 panoramic lenses of Corona satellites moved through a 70° arc perpendicular to the direction of orbit. To capture stereoscopic images, both front and back cameras had a 15° tilt forward and backward, respectively. The orbit altitudes were approximately 180–185 km, and the resolution varied across image, ranging from 2.7 to 7.6 m with the finest located in the center. The images are providing 70% overlap between consecutive image frames and were scanned with 7 μm resolution. We analyzed both forward- and backward-facing photographs as separate sets, and jointly by concatenating the two images into one with two bands, and tested if the combination of the two bands resulted in an improvement in classification accuracy. Because our imagery was recorded in October, >20,000 km² area (about 12.9% of our study area) was covered by snow. During summer, many of these areas, especially right above the treeline are not covered by snow, but by October, winter had already arrived in the mountains. Our source of digital elevation data was the Shuttle Radar Topography Mission (SRTM) (Farr et al., 2007). We present our workflow in Fig. 2 and the processing environments for each step in Table S1.

2.3. Orthorectification

We acquired 59 scanned Corona images from the United States Geological Survey (USGS, 2019). Each image covered an area of approximately 17 × 232 km. To orthorectify the images, we applied

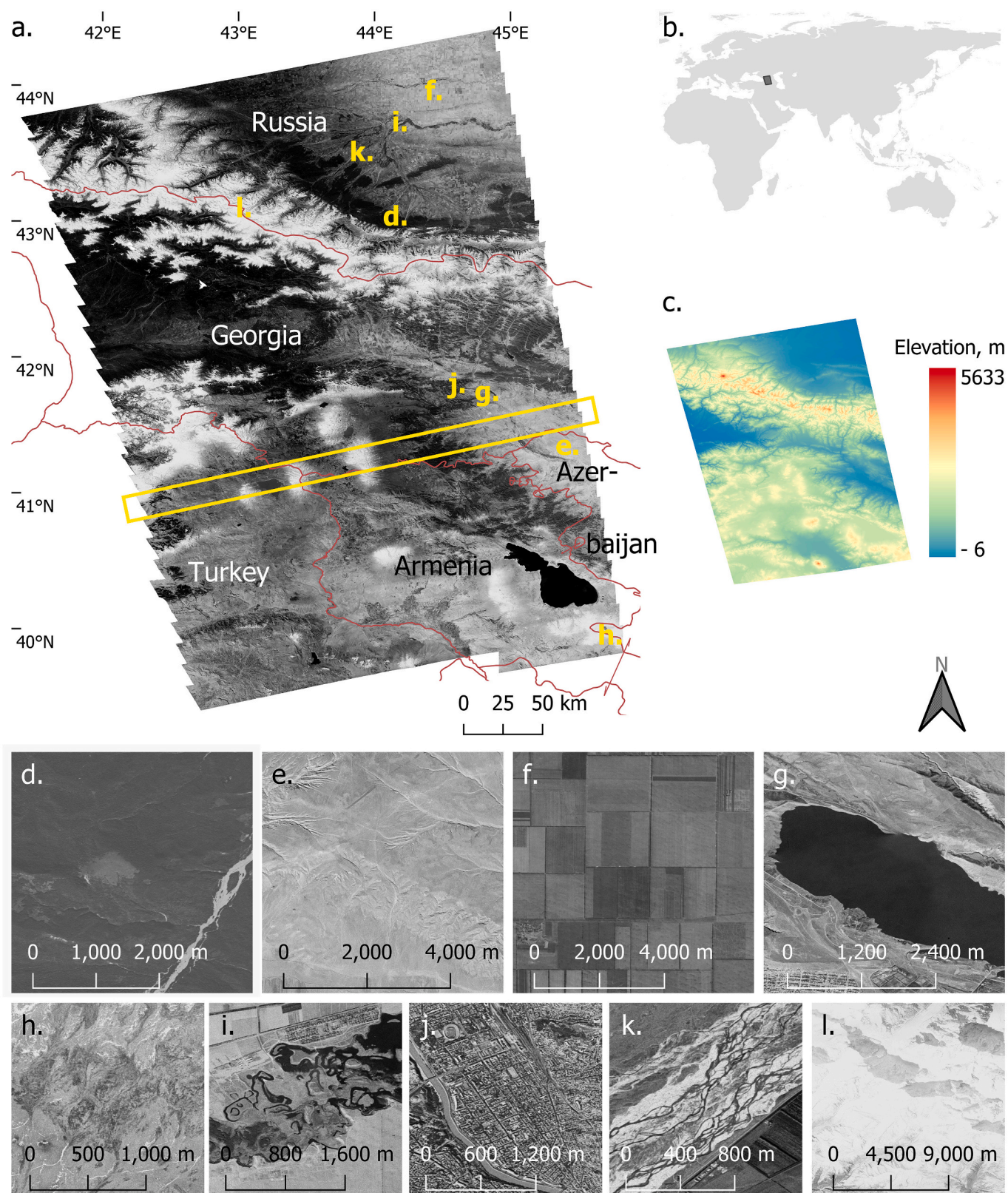


Fig. 1. a. Study area in the Caucasus ecoregion, which includes parts of Russia, Armenia, Azerbaijan, Georgia and Turkey, with one Corona image strip highlighted in the yellow frame; b. Location of the study area on a world map; c. Elevation map in the study area; and zoomed in examples of our different land cover classes d. forest; e. grassland; f. cropland; g. lake; h. barren; i. wetland; j. urban; k. river; l. snow-and-ice. The location of these examples are indicated with yellow letters in the full Corona image. (For interpretation of the references to colour in this figure legend, the reader is referred to the web version of this article.)

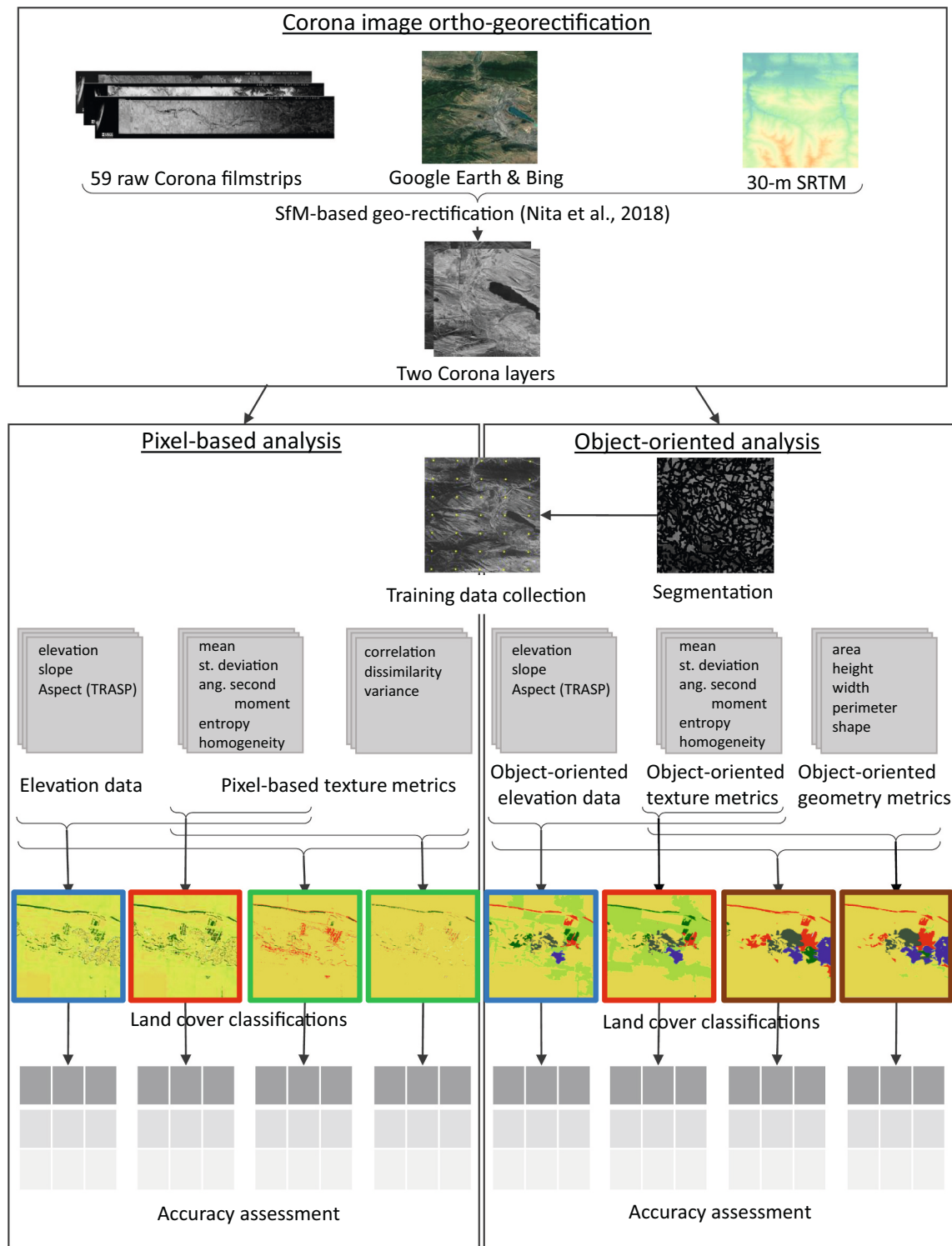


Fig. 2. Flowchart of the pixel-based and object-oriented land cover classification procedure. In the row of the different land cover classifications we highlight that we compared to each other in different colors. In blue are the pixel-based and object-oriented classifications with five texture metrics, in red those with five texture metrics and elevation information. We also highlight in green the pixel-based classifications with eight texture metrics with and without elevation information, respectively; and in brown the object-oriented classifications with five texture metrics and five object geometry information metrics with and without elevation information. Additionally, we present the processing environments for each step in Table S1. (For interpretation of the references to colour in this figure legend, the reader is referred to the web version of this article.)

Structure from Motion (SfM) algorithms (Song et al., 2015; Ullman, 1979) and the Corona georectification approach developed by Nita et al. (2018) in AgiSoft Metashape software (AgiSoft, 2021). First, we co-aligned the raw strips and generated a point cloud. Second, we

assigned coordinates to this point cloud based on high-resolution Google Earth and Bing imagery and generated orthophotos with 2.5 m resolution. During the mosaicking, the processing pipeline implements a data division approach, which splits the data into several frequency domains,

which are blended independently. The highest frequency component is blended along the seamline only, and each further step away from the seamline results in a lower number of domains being subject to blending. Therefore, any differences (e.g., due to the effect of the bidirectional reflectance distribution function [BRDF]), which were still persistent after image normalization between overlapping images, were removed by these steps. We grouped the 59 raw images into 30 pairs, given the decreasing overlap between the forward and backward stereo-medium photographs. Unfortunately, because the images were only 'stereo-medium', we could not extract a high-resolution continuous digital surface model from the Corona data, but only the one with gaps in areas where the raw photographs did not overlap, so we used instead the SRTM to generate the orthophotos (Nita et al., 2018). When processing mosaics from a sequence of Corona stereo images, there are two types of overlap: the overlap between successive frames of a Corona camera, and the overlap between the two images of the stereo pair. In our imagery, there was an overlap of approximately 8% between successive frames at the center of the format, which relates directly to the camera scan rate, which is determined by the ratio of the satellite velocity to its height above ground (NRO, 1967). The overlap within the stereo pairs varies somewhat among acquisitions and with orbital elevation but is typically approximately 90% for stereo photographs named in metadata as 'stereo-high' and approximately 70% for 'stereo-medium' (USGS, 2019). Our data were stereo-medium and that meant that the successive stereo images have little overlap, which results in a small overlap between their DEMs (Goerlich et al., 2017). Therefore, only 30 pairs could be formed. However, this did not affect our SfM procedures because the pairs were processed separately and bundle adjusted in the end, according to methodology published by Nita et al. (2018). As demonstrated in previous studies (Nita et al., 2018; Rendenieks et al., 2020) an average of 20–26 independent check ground control points (GCP) per strip is sufficient for an accurate orthorectification, but this number depends somewhat on topography, clouds, and image characteristics (e.g., sharpness, illumination, etc.). We selected the GCPs as visible points (e.g., crossroads, visible landmarks etc.) that did not change over time. Accordingly, we assessed the root mean square errors of the resulting images using an average number of 26 GCPs per stereographic pair, for a total of 802 GCPs.

2.4. Pixel-based classification

For our pixel-based supervised land cover classification, we calculated the first- and second-order texture metrics. Second-order texture metrics were based on the grey-level co-occurrence matrix (GLCM, *glcmTexture*). We set the offset distance of the GLCM textures calculated within Google Earth Engine (GEE) platform at the default of one pixel and retained the original quantization of 8 bits. We calculated the second-order texture metrics over east-west and north-south directions and averaged those for each metric to create single multi-directional texture metrics. In order to determine the best window size for the texture calculation, we conducted tests in several smaller subsets of our study area with variety of elevations and land cover types using 3×3 and 7×7 pixel windows. We selected the 7×7 window size because differences between different land cover types were more distinct than for the 3×3 window size. Validation of the classification maps for those subset areas using 3×3 and 7×7 window size resulted in overall accuracies of $69.5 \pm 5.0\%$ and $70.2 \pm 5.3\%$, respectively. To compare the pixel-based and object-oriented classifications, we calculated mean and standard deviation as first-order metrics, and angular second moment, entropy, and homogeneity as second-order texture metrics, all within 7×7 pixel windows (Conners et al., 1984; Haralick et al., 1973), and used these for a first classification. To test if they would improve the pixel-based classifications, we also calculated second-order texture metrics of correlation, dissimilarity, and variance (Farwell et al., 2021) for a second classification.

We performed pixel-based Random Forest classifications (.*smileRandomForest*)

setting the tree size to 100 and applied a 10-fold Monte Carlo (Picard and Cook, 1984) Random Forest classification with majority voting (Cui et al., 2018). Ten folds are most commonly used (Ruiz Hernandez and Shi, 2017; Song et al., 2017), because it ensures a sufficient number of folds and sufficient number of training points in each fold (Kuhn and Johnson, 2013; Molinaro et al., 2005). We calculated metrics, and conducted the Random Forest classification in GEE (see below, Gorelick et al., 2017). To determine how important each of the chosen metrics (Table S2) were for our classification, we ran importance tests within R software (R Core Team, 2022) and calculated the mean decrease in accuracy, which represents the difference in overall accuracy if a given metric is removed.

2.5. Object-oriented classification

For our object-oriented supervised classification, we also applied a 10-fold Monte Carlo (Picard and Cook, 1984) Random Forest classification with majority voting (Cui et al., 2018) within GEE (.*smileRandomForest*) setting the tree size to 100. Prior to the classification, we performed the segmentation (described in the following section) and calculated the objects' geometry information: area, perimeter, width, height (Gorelick et al., 2017), shape (Li et al., 2007; Nghi and Mai, 2008), as well as the texture. The width and height were calculated based on the bounding box. We calculated object-oriented first- (mean and standard deviation), and second-order texture metrics (angular second moment, entropy, and homogeneity) by applying the same texture calculation parameters as in pixel-based classification (Conners et al., 1984; Farwell et al., 2021; Haralick et al., 1973), but with a 7×7 pixel moving window within each object obtained from the segmentation. We clipped the original images by the segment borders and applied a 7×7 moving window. Along the edges of segments where the windows extended beyond the segment boundaries, we treated outside pixels as 'no data', and calculated texture metrics for the inside pixels only. We also summarized the elevation data for the objects obtained during the segmentation. We conducted one classification using only the texture metrics so that we could compare that classification with the pixel-based classification, but also performed an object-oriented land cover classification that also included the object geometry information to test whether it would help improve the final accuracy results. Again, we calculated importance of metrics based on the mean decrease in accuracy for each scenario.

2.5.1. Segmentation

We performed image segmentation in order to outline image objects prior to our classifications (Haralick et al., 1973; Kressler et al., 2003). For the segmentation, we used the Simple Non-Iterative Clustering (.*SNIC*) algorithm (Achanta and Süsstrunk, 2017). The SNIC algorithm is computationally efficient, while allowing control over the number and compactness of output segments (Achanta and Süsstrunk, 2017). The compactness parameter represents the ratio between a segment's perimeter and square root of its area (Happ et al., 2010). We performed the segmentation within GEE.

Classification results of object-oriented classifications depend on the quality of segmentation (Blaschke, 2010; Clinton et al., 2010; Kavzoglu, 2017; Kavzoglu and Tonbul, 2018), and hence how segmentation parameters are set. We selected the segmentation parameters after conducting numerous tests in a variety of altitudes and land cover types. We present the results of these tests in Table S3. The selected parameters were best in merging the information of each land cover class into a separate segment. We set the distance between the seeds represented by 'seed grid' parameter to 40 pixels, the connectivity parameter to 4 neighbors, and the compactness factor at 0.1, which ensured a low ratio of the area of a segment to its perimeter (Achanta and Süsstrunk, 2017). This avoided overly convoluted segments. We quantified the segmentation results by separating the objects into four categories: homogeneous segments (100% of the dominant class); segments with 75–100%

of the dominant class; segments with 50–75% of the dominant class and segments with several classes (no class covering 50%) (Table S4). The segments were the objects for our object-based classification, and we use the two terms ‘segment’ and ‘object’ synonymously.

2.6. Training and validation data

To collect both our training and our validation data, we applied a systematic sampling design and generated a 5×5 km point grid of 4828 points for our study area. We opted for a systematic sampling design to limit the effects of spatial autocorrelation by maximizing the distances between points, and to ensure that all countries and ecoregions in our study area had the same sampling density. Our systematic sampling design is comparable to the sampling design for the LUCAS land use

dataset of the European Union (LUCAS, 2022). We based our choice of distance between points in the grid on the need to balance the advantage of a higher sample size, with the feasibility of collecting the data. We used Corona data for each point to visually identify the dominant land cover class of the segment the point belonged to, and assigned the dominant class in the segment to the grid point. The high resolution of the Corona imagery allowed unambiguous visual differentiation between the classes in almost all cases (Fig. 1). All points were labeled by one expert (A.R.) for consistency. The point grid took approximately one month of full-time work to classify into forest, grassland, cropland, barren, wetland, urban, river, lake, and snow-and-ice (Fig. 1, Table S5). We also determined if segments included more than one class (e.g., Fig. 3). We removed grid points in such segments from the training data, but retained them if they were part of the validation dataset (see below).

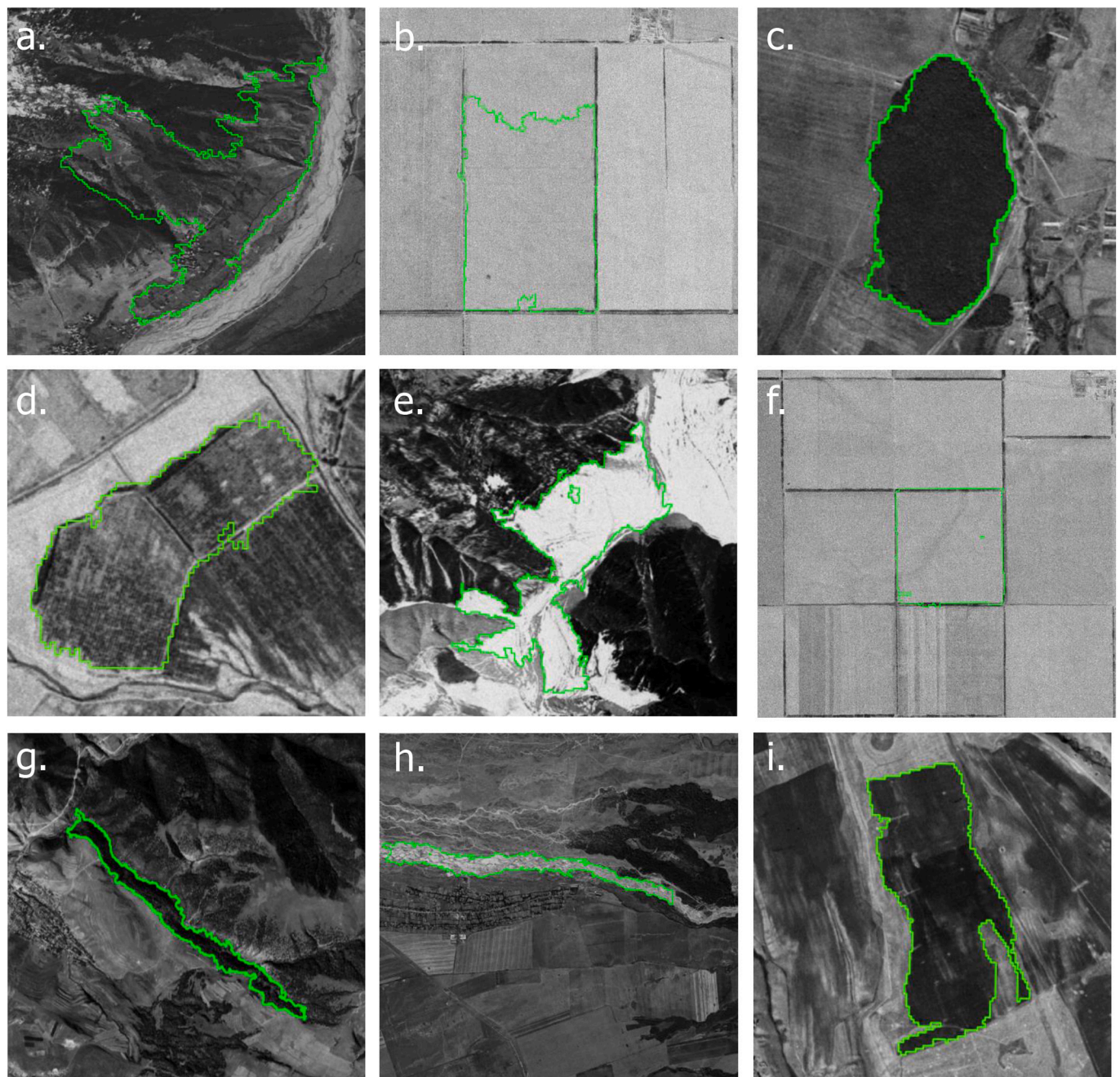


Fig. 3. Results of the SNIC segmentation algorithm on the panchromatic Corona imagery. Shown are examples of a heterogeneous segment that is over-segmented (a); and homogeneous segments that are under-segmented (b), or correctly segmented (c-i).

For classes that were rare, or were misclassified in initial runs, we manually added training points (Table 1, Table S4) but did not use these added points for validation. Thus, we had 5126 points total for training and validation. We used the same training and validation data for both the pixel-based and object-oriented classifications.

For training, we used 80% of the points located in homogeneous segments, as well as the additionally collected training data. For validation, we used the remaining 20% of the points associated with homogeneous segments, plus 20% of the points within heterogeneous – missegmented or shifted objects. Some of the missegmented or shifted objects occurred due to errors in orthorectification so that the two concatenated images captured by forward- and backward-facing camera did not co-align perfectly. For our accuracy assessment, we used 10-fold validation from randomly split training and testing data. We did not manually add points to the validation dataset. These steps resulted in 10 sets, each totalling 3684 points: 2719 for training and 965 for validation. In order to determine whether the number of the points was sufficient for our classifications, we ran tests with fewer points. Namely, we selected 66% and 50% of both the training (1795 and 1360) and validation (637 and 483) points to classify our land cover and calculate map accuracies. The rationale was that if accuracies for the smaller subsets are similar to that for the full set, then that suggests that the full set was sufficiently large and more points would not have improved classification accuracy greatly. We used the same 10 sets of training and validation points for both the pixel-based and the object-oriented classifications, so that the individual training pixels were only derived from homogeneous segments.

2.7. The effect of the DEM

To test the effect of adding elevation data on classification accuracy, we resampled the 30-m SRTM elevation model to 2.5-m to match the remaining metrics using nearest neighbor resampling method, and calculated slope and aspect. To overcome the problem that when calculating aspect, the two opposite ends of the range both refer to North, we normalize the aspect variable by calculating topographic radiation aspect index (TRASP) proposed by Maxwell and Shobe (2022) (Table S2). We then added slope and TRASP plus elevation as input metrics for both the pixel-based and object-oriented classifications. For our classifications of the Corona imagery plus the elevation data, we followed all the steps described above, and used the same sets of training and validation data.

2.8. Validation, accuracy assessment

We conducted a thorough accuracy assessment of the resulting land cover maps and calculated the overall accuracy, user's accuracy and producer's accuracy following the best practices outlined in Olofsson et al. (2014). To capture variability among classifications, we calculated their standard deviation. Because the barren, wetland, urban, and river classes covered only small portions of our study region and had often only a few validation points, we merged them into one class named 'others' when reporting the accuracies, but retained them as separate classes in our maps for visualization purposes.

Table 1
Number of points in our training and validation datasets. For each of our 10 Random Forest classifications, training and testing points were randomly selected from the four different pool of grid points. For the number of points in each land cover class, please see Table S4 in the supplementary material.

	Total	Training	Testing
Grid points in homogeneous segments	3026	2421 (80%)	605 (20%)
Additional points	298	298 (100%)	0 (0%)
Grid points in shifted segments	915	0 (0%)	183 (20%)
Grid points in missegmented objects	887	0 (0%)	177 (20%)
Total	5126	2719	965

3. Results

We successfully produced high-resolution land cover maps from 1964 Corona imagery for our study area with nine major land cover classes (forest, grassland, cropland, lake, and snow-and-ice), plus four minor land cover classes (barren, wetland, urban, and river), which we grouped into 'others' for our accuracy assessment.

3.1. Orthorectification

Our orthorectification of the scanned Corona satellite images from 1964 was highly accurate. Based on our 802 independent check ground control points, our geo-rectification had an absolute root mean square error of 16.3 ± 10.4 m. Co-registration errors were highest in areas with few stable ground features, such as buildings, rivers, and road intersections (Fig. 4). Contrary to what we had expected, co-registration errors were not higher in the more mountainous parts of our study area.

3.2. Importance tests for metrics

Our importance tests showed that the most important metrics for the classifications were similar for all pixel-based and object-oriented classifications (Table 2). The most important were the mean of both panchromatic bands (6.6–9.6% and 7.4–11.3% decrease in overall accuracy if the mean of backward-facing camera and forward-facing camera images were removed), and slope (6.8–12.6%). The least important were the object geometry metrics included for the object-oriented classification (0.9–2.0%), but they still improved the overall accuracy.

3.3. Pixel-based classification of Corona imagery

Our supervised pixel-based classification with five texture metrics (Fig. 5, Fig. 6) had an overall accuracy of $63.0 \pm 5.0\%$ (Fig. 7, Table 3, Table S6). Classification accuracy was lower for grasslands, croplands

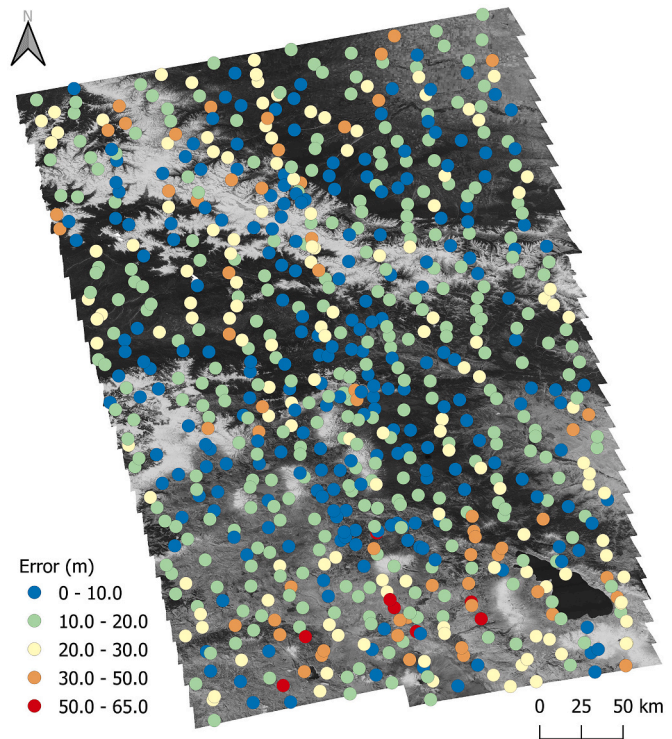


Fig. 4. Distribution of the ground control points for the orthorectification and their locational error after the rectification.

Table 2

Importance of the metrics that we employed for the pixel-based and object-oriented land cover classifications for Corona satellite images captured by backward (B1) and forward (B2) camera. All texture metrics were calculated with a moving window size of 7×7 pixels.

Metrics		Mean decrease in accuracy (%) for:							
		Pixel-based classification				Object-oriented classification			
		with five textures	with five textures and DEM	with eight textures	With eight textures and DEM	with five textures	with five textures and DEM	with five textures and object geometry information	with five textures, object geometry information and DEM
First-order textures	Mean Panchromatic B1	9.6	8.6	7.4	6.8	9.4	8.5	7.3	6.6
	Mean Panchromatic B2	11.3	9.8	8.5	7.5	11.0	8.9	8.5	7.4
	Standard deviation B1	3.4	3.7	2.3	2.6	4.5	4.0	3.3	2.7
	Standard deviation B2	2.3	2.6	1.7	1.8	4.2	4.0	3.0	2.7
	Angular second moment B1	2.8	2.9	1.8	2.0	6.5	6.0	4.9	4.4
	Angular second moment B2	2.6	2.6	1.8	2.1	7.2	6.4	5.2	5.0
GLCM-derived second-order textures	Entropy B1	2.8	2.9	1.8	2.1	6.3	6.0	4.9	4.4
	Entropy B2	2.6	2.7	1.9	2.1	6.6	6.5	5.0	5.0
	Homogeneity B1	2.7	2.8	1.9	2.1	6.6	5.7	4.6	4.4
	Homogeneity B2	2.8	3.0	1.9	2.3	6.9	6.5	5.4	4.9
	Correlation B1*			1.1	1.1				
	Correlation B2*			0.6	0.6				
	Dissimilarity B1*			1.9	2.2				
	Dissimilarity B2*			1.8	2.2				
	Variance B1*			2.0	2.3				
	Variance B2*			1.5	1.8				
Elevation data	Elevation		7.8		5.9		8.5		6.6
	Slope		8.6		6.8		12.6		9.8
	TRASP (topographic radiation aspect index)		1.5		1.1		2.8		2.1
	Area**	NA	NA	NA	NA			1.8	1.5
Object geometry	Height**	NA	NA	NA	NA			1.1	0.9
	Width**	NA	NA	NA	NA			1.7	1.3
	Perimeter**	NA	NA	NA	NA			2.0	1.6
	Shape**	NA	NA	NA	NA			1.4	1.2

* Calculated additionally for pixel-based classification.

** Object-based metrics not applicable (NA) for pixel-based classification.

and lakes with $57.8 \pm 9.0\%$, $54.7 \pm 7.3\%$, and $41.4 \pm 8.1\%$ UA, and $46.4 \pm 6.7\%$, $55.6 \pm 8.4\%$, and $67.5 \pm 14.9\%$ PA, respectively. In contrast, the accuracies for forest ($68.5 \pm 3.8\%$ UA and $78.0 \pm 2.4\%$ PA) and snow-and-ice ($85.0 \pm 4.2\%$ UA and $87.2 \pm 3.4\%$ PA) classes were considerably higher but they were sometimes confused with shadows in mountainous areas. The 'others' class, which included barren, wetland, urban, and river had low accuracy, but also covered only small areas within our study region.

3.4. Object-oriented classification of Corona imagery

3.4.1. Segmentation

Our optimal segmentation parameters resulted in objects of $0.75 \pm 0.52 \text{ km}^2$ on average. We checked the quality of segmentation visually (Zhang et al., 2008) and found it overall to be accurate. We found that approximately 18.4% of the assessed objects (887 out of 4828 total) were missegmented and included more than one land cover class (Table 1, Table S4). Segmentation errors mainly occurred when there was high similarity in spectral signature between different classes, and sometimes when there were mis-registration problems between the forward and backward photos (915 out of 4828 total, Table 1, Table S4).

3.4.2. Classification

The supervised object-oriented classification with five texture metrics using Random Forest algorithm (Fig. 5, Fig. 6) yielded an overall accuracy of $67.3 \pm 4.0\%$ (Fig. 7, Table 3, Table S6). The forest, lake and

snow-and-ice classes had the highest accuracies ($72.6 \pm 3.0\%$, $74.9 \pm 9.0\%$ and $88.5 \pm 2.5\%$ UA and $80.4 \pm 2.2\%$, $84.1 \pm 7.2\%$ and $87.0 \pm 2.7\%$ PA, respectively). The grassland and cropland classes had the lowest accuracies ($58.9 \pm 8.3\%$ and $62.8 \pm 6.2\%$ UA and $58.5 \pm 4.6\%$ and $55.6 \pm 8.8\%$ PA, respectively), largely because those two classes were frequently confused. Again, the 'other' class was not well classified.

As a test, in a subset area we conducted the classifications for each band separately, and for both bands together. We found an improvement of about 2 percentage points in overall accuracies when classifying both bands together ($77.6 \pm 2.4\%$), compared to the single-band classifications ($75.6 \pm 3.2\%$ for forward- and $75.7 \pm 2.7\%$ for backward-facing camera image). In all of these comparisons, we conducted object-oriented classifications, and included the DEM and object geometry information.

3.5. Pixel-based vs object-oriented classification of Corona imagery

The object-oriented classification had higher overall and user's accuracies for each class than the pixel-based classification (Fig. 7, Table S6). The greatest improvement in class-level accuracies were for grassland, cropland, and lake classes. Both the pixel-based and object-oriented classifications had similar spatial patterns (Fig. 5). Croplands were dominant in the northeastern portion of our study area in both classifications. However, some classes, such as the snow-and-ice, were noticeably less common in the pixel-based classification. The forest class was better mapped in the object-oriented classification, especially in

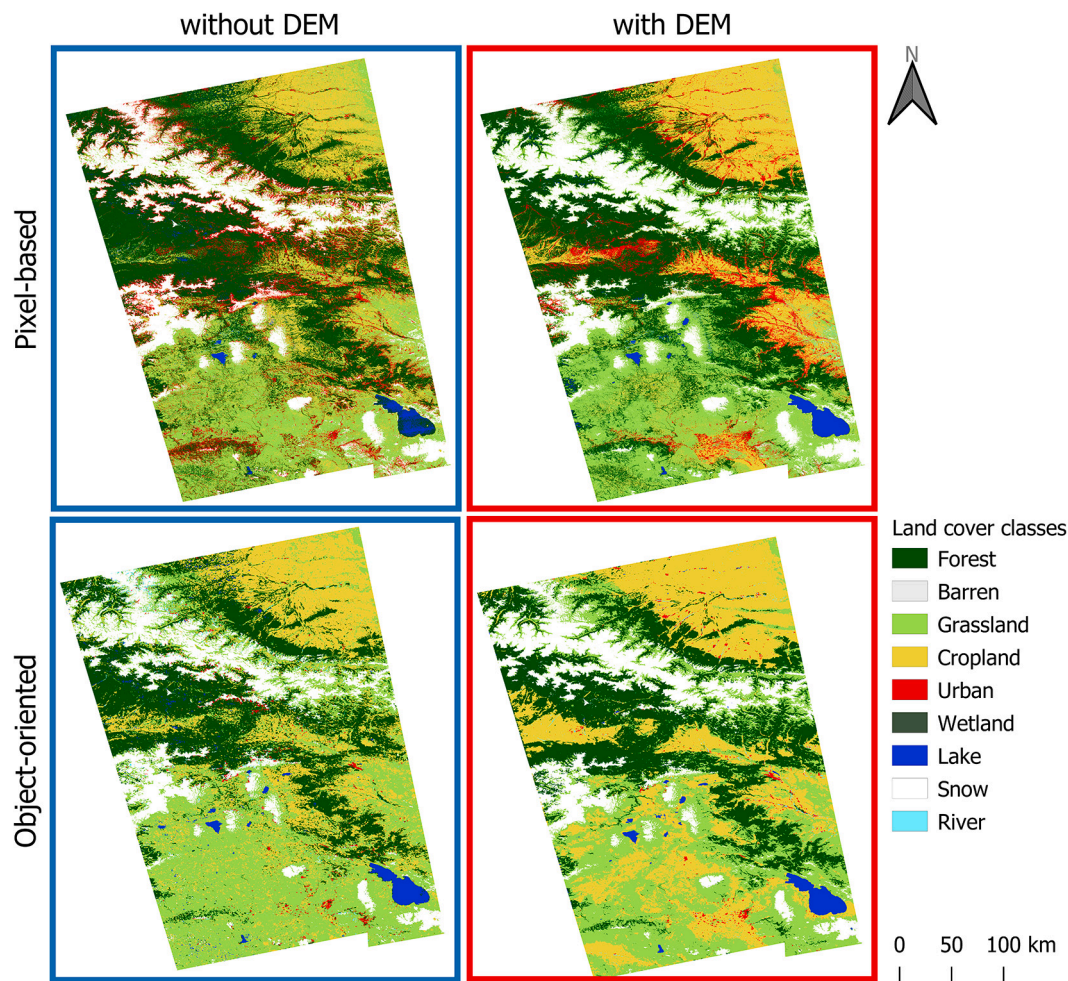


Fig. 5. Our 1964 land cover maps for comparison of pixel-based and object-oriented classification methods. Highlighted in blue are classifications with five texture metrics, and in red those with five texture metrics and elevation information. (For interpretation of the references to colour in this figure legend, the reader is referred to the web version of this article.)

mountainous areas bordering snow-and-ice.

3.6. Classifications of Corona imagery plus DEM

Adding the DEM to both the pixel-based and object-oriented land cover classifications (Fig. 5, Fig. 6) increased overall accuracies to $75.3 \pm 3.0\%$ and $78.7 \pm 2.5\%$, respectively (Fig. 7, Table 3, Table S6). Inclusion of the DEM resulted in an increase of UA and PA of almost all land cover classes both for pixel-based and object-oriented classifications. The greatest improvements were in the lake class, which increased in UA from $41.4 \pm 8.1\%$ to $89.1 \pm 6.0\%$ and in PA from $67.5 \pm 14.9\%$ to $92.5 \pm 4.1\%$ in pixel-based classifications and from $74.9 \pm 9.0\%$ to $94.4 \pm 5.2\%$ in UA and from $84.1 \pm 7.2\%$ to $95.2 \pm 4.9\%$ in object-oriented classifications. Similarly, when including the DEM, the cropland class had an increase in user's accuracy by 19.4 and 13.4 percentage points, and in producer's accuracy by 18.7 and 25.5 percentage points, in the pixel-based and object-oriented classifications, respectively. However, accuracy of snow-and-ice land cover class did not change noticeably ($\sim 85\text{--}91\%$ in land cover maps from both classifications). Our accuracy assessment using only the grid points associated with homogeneous segments (Table 1, Table S4) yielded overall accuracies of $75.8 \pm 2.1\%$ and $81.7 \pm 1.7\%$ for pixel-based and object-oriented classifications, respectively.

Our experiments using only 50% and 66% of the training and validation data for the object-oriented classification with DEM resulted in

overall accuracies of 74.4% and 75.8%, respectively. This is quite close to the accuracy of 78.7% for the full dataset and suggests that accuracy had stabilized with our 3684 points and would not have increased substantially with a larger training dataset.

Our object-oriented classification with the incorporation of the DEM also resulted in the classification that made visually the most sense. The greatest improvement occurred in areas of misclassification among spectrally similar classes, such as forest vs. lake, snow-and-ice vs. urban, as well as in cast shadow areas, which can make snow and grass in the high mountains appear dark. Thus, in our resulting map with highest overall accuracy (object-oriented with five textures and DEM), forest comprised 27.0%, grasslands – 30.4%, croplands – 27.5%, lakes – 1.3%, snow-and-ice – 12.9%, and others – 0.9% of the total study area.

Our additional pixel-based classifications (Fig. 6, Fig. 8), with eight texture metrics did not improve our accuracy results by yielding only $62.8 \pm 5.0\%$ and $74.4 \pm 2.9\%$ with and without DEM (Fig. 7, Table 3, Table S7). Similarly, we did not observe an improvement in object-oriented classifications when including the object geometry information (Fig. 6, Fig. 8). The overall accuracies with and without DEM were $67.9 \pm 4.2\%$ and $78.6 \pm 2.2\%$, respectively (Fig. 7, Table 3, Table S7).

4. Discussion

We developed a new approach to conduct large-area land cover classifications from single-date, 2.5 m resolution panchromatic Corona

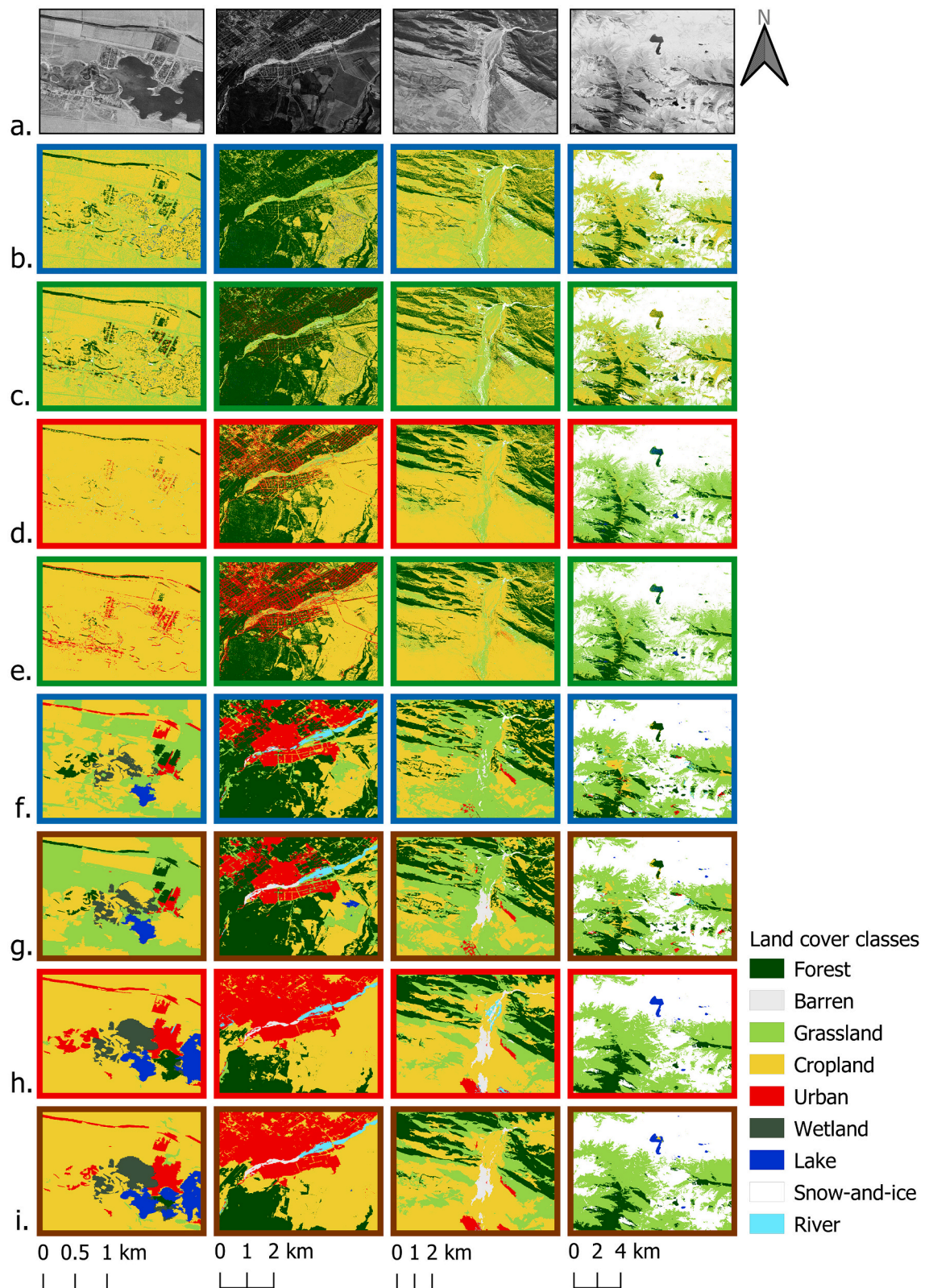


Fig. 6. Zoomed in examples of a. original Corona imagery followed by the results of pixel-based classifications with: b. five (mean, standard deviation, angular second moment, entropy, homogeneity) and c. eight texture metrics (plus correlation, dissimilarity, variance) without DEM; and d. and e. with DEM; object-oriented classifications with: f. five texture metrics, g. plus object geometry information without DEM; and h. and i. with DEM. We compared the pairs highlighted in red frame to each other, as well as the pairs highlighted in blue frame. (For interpretation of the references to colour in this figure legend, the reader is referred to the web version of this article.)

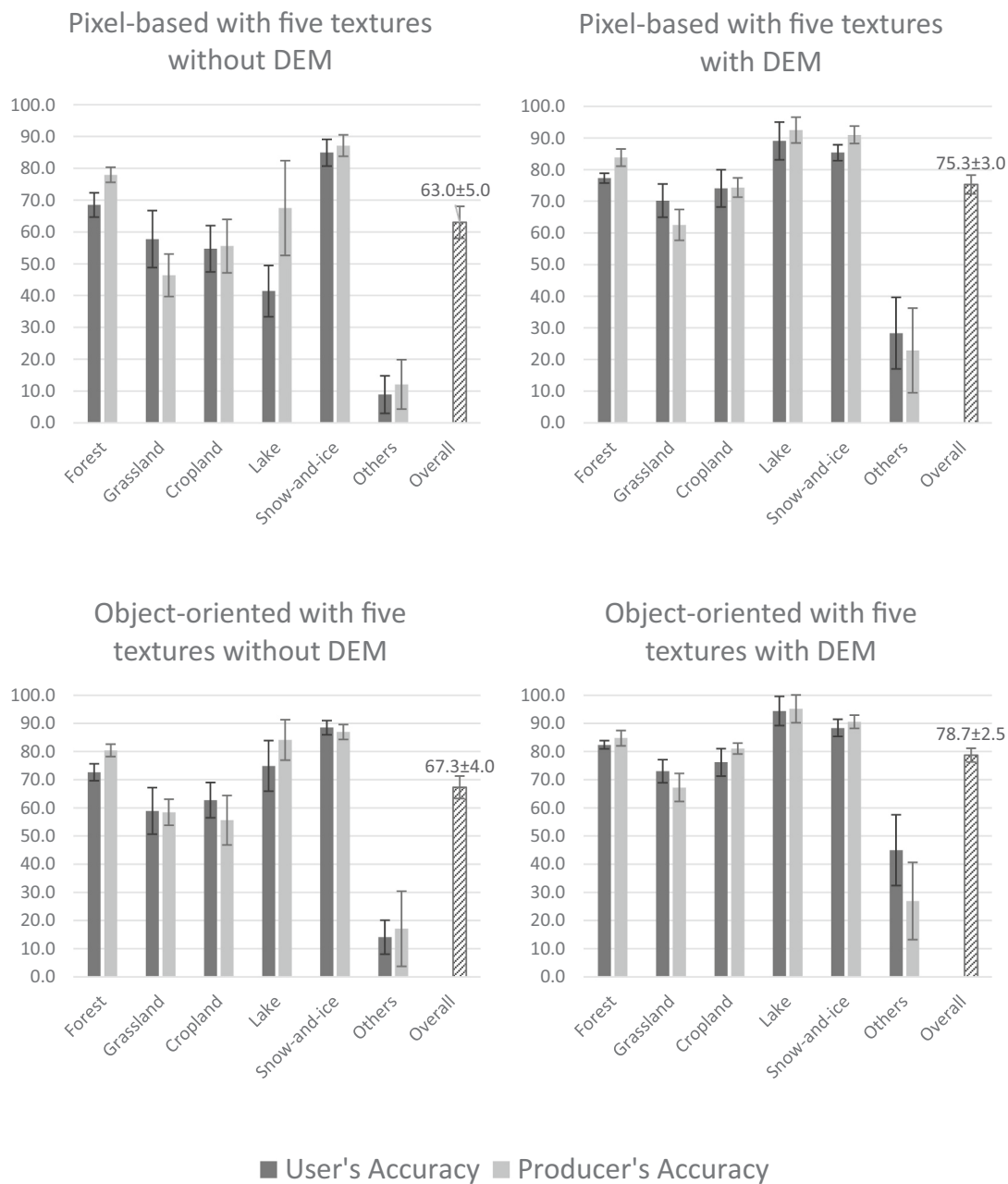


Fig. 7. Histograms of the user's and producer's accuracy of each land cover class and the overall accuracy for the pixel-based and object-oriented classifications with and without the DEM. The 'error' bars represent the standard deviation.

satellite imagery for 1964. We calculated both pixel-based and object-oriented metrics, from which we derived our land cover maps. Our object-oriented classification outperformed the pixel-based classification, and classification accuracy was even higher when including a DEM ($78.7 \pm 2.5\%$ overall accuracy). Ultimately, we showed that it is possible to conduct automated classifications from single-date panchromatic imagery for a full suite of land cover classes in large areas from high-resolution 1964 spy satellite imagery, thereby providing land cover information several decades prior to what is possible from multi-spectral earth observing satellites.

For the science of land use, it is important to develop robust methods to map land cover from 1960s Corona satellite data in order to expand the length of time series for land cover and land use change detection. Corona satellite images can extend the temporal baseline for land use

studies to the mid-20th century. This allows capturing important historical events, such as the peak of the Cold War between the USA and the USSR (McMahon, 2021), the green revolution (Evenson and Gollin, 2003), as well as the continued expansion of mechanization and industrialization of agriculture (Crossley et al., 2021). Our study period also includes the era when human populations grew most rapidly (United Nations, 2019), which resulted in increased food demand and thus agricultural production. Thus, to evaluate the long-term effects of these historical events, Corona satellite images provide unique information for land use science.

There have been a handful of studies using the Corona spy satellite imagery for land cover classification but no study was conducted for a large area and a full suite of land cover classes. Some of the previous studies used pixel-based classification (Song et al., 2015) or object-

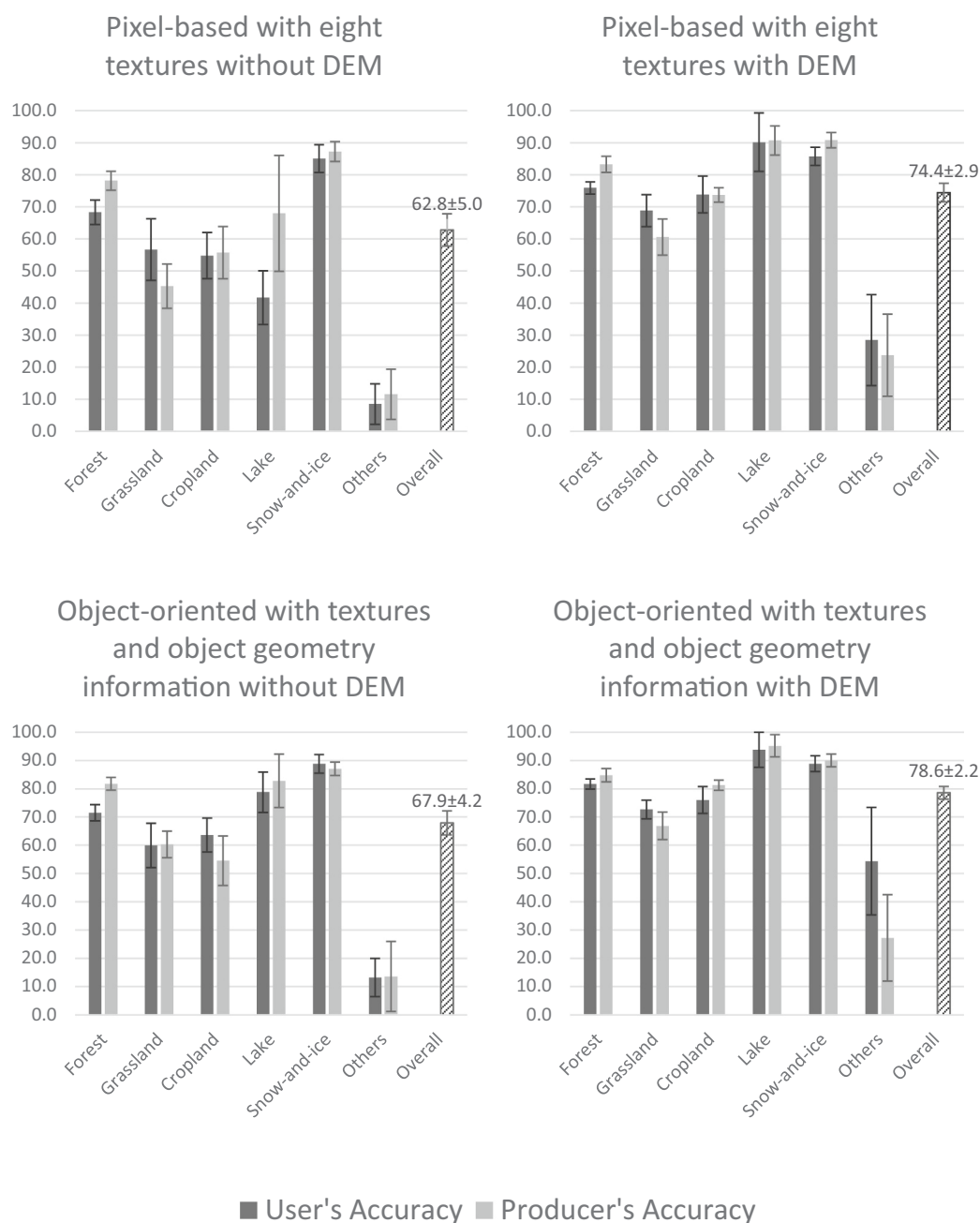


Fig. 7. (continued).

Table 3

Overall classification accuracy with confidence intervals resulting from each of the different set of input variables.

Classification scenarios			Overall accuracy
Pixel-based classifications	1	with five textures	63.0 ± 5.0%
	2	with five textures and DEM	75.3 ± 3.0%
	3	with eight textures	62.8 ± 5.0%
	4	with eight textures and DEM	74.4 ± 2.9%
Object-oriented classifications	5	with five textures	67.3 ± 4.0%
	6	with five textures and DEM	78.7 ± 2.5%
	7	with five textures and object geometry information	67.9 ± 4.2%
	8	with five textures, object geometry information and DEM	78.6 ± 2.2%

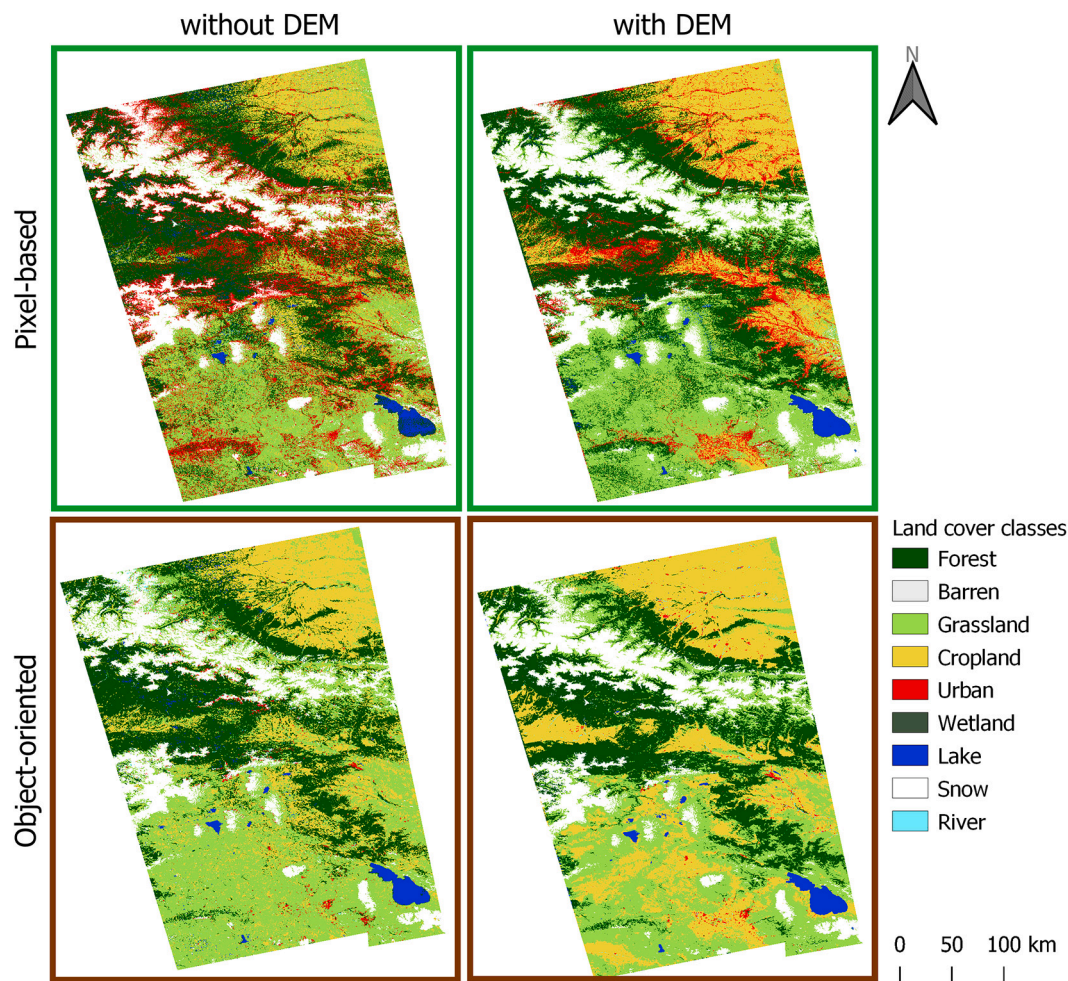


Fig. 8. Our additional 1964 land cover maps produced in an attempt to improve the classification results for highlighted based on each method. In green are the pixel-based classifications with eight texture metrics with and without elevation information. In brown are the object-oriented classifications with five texture metrics and five object geometry information metrics with and without the elevation information. (For interpretation of the references to colour in this figure legend, the reader is referred to the web version of this article.)

oriented classification for forest vs. non-forest (Rendenieks et al., 2020) and for smaller study areas (e.g., $\sim 30 \text{ km}^2$ in Shahtahmassebi et al., 2017). The results of our land cover classification ($78.7 \pm 2.5\%$, $158,000 \text{ km}^2$) compare favorably with the previous results of Corona imagery classifications for smaller study areas (93% for $22,400 \text{ km}^2$ in Gurjar and Tare, 2019), and forest-non-forest classifications ($\sim 95.5\%$ in Song et al., 2015; $\sim 90\%$ in Song et al., 2021; $\sim 92\%$ in Rendenieks et al., 2020). Our pixel-based classification yielded $75.3 \pm 3.0\%$, which is comparable to accuracies of other studies using a pixel-based approach, but for two land cover classes only and smaller areas (95% for $\sim 770 \text{ km}^2$ and 96% for 1240 km^2 in Song et al., 2015).

In general, there are few automated land cover classifications derived from high-resolution imagery that cover large areas (Khare and Ghosh, 2016). Similarly, automated classifications from Corona imagery are rare, and many of the previous studies applied a considerable amount of manual effort and hand digitization (Dittrich et al., 2010; Ruelland et al., 2011; Zhang et al., 2020). Our methodological advancement allowed for an efficient regional-scale land cover mapping of single-date 2.5-m panchromatic Corona imagery. We automated the classification process deriving a combination of texture and geometry metrics and classification along with the rigorous validation of the resulting maps. By ‘automated land cover classification’ we refer to the set of codes available freely on Google Earth Engine platform and GitHub (<https://github.com/rizayeva/coronaClassification.git>). Our codes can be used for a different sets of very high-resolution

panchromatic imagery, and parameters that need to be adjusted are noted in the code description. We were able to overcome some issues caused by availability of only the single-date imagery, and we reached a classification accuracy of up to $78.7 \pm 2.5\%$. We attribute the high accuracy to our use of a combination of second-order texture metrics, as well as elevation information. However, because we analyzed only one image, and that image was from October, there was some misclassification between the cropland and grasslands, which we had expected, and also croplands and forests, which surprised us. The reason why grasslands and croplands were not always correctly distinguished from each other is that neither have green vegetation in our study area in October, making it difficult to delineate crop fields from other classes in panchromatic images, especially when compared to spectrally rich satellite images (Wardlow and Egbert, 2003). This was especially a problem in our pixel-based classification, and we could remedy this issue partly in the object-oriented classification via the objects’ geometry information metrics. The confusion of croplands with forests occurred because the pixels with some freshly ploughed winter crop fields had low values, similar to forests. Our work focused on Corona spy satellite data with only two panchromatic images captured, one by forward- and one by backward-facing camera. For the modern era, higher classification accuracies are possible with multi-spectral imagery, but for the 1960s, there are no other data, and that makes Corona imagery and our land cover classification approach valuable. As more high-resolution imagery becomes available with new commercial satellites with comparably rich

spectral information, our methods for classifying the large areas with Corona imagery may also be relevant for other high-resolution satellite images.

We found that our pixel-based and object-oriented classifications each had some costs and benefits. The pixel-based classification had considerably lower accuracy, and resulting maps had a ‘salt-and-pepper’ pattern. This may necessitate a substantial amount of post-classification noise removal (Zheng et al., 2014). However, the pixel-based classifications ran much faster (Duro et al., 2012), and did not require image segmentation and per-object texture calculation. The object-oriented classification had higher accuracy, but accuracies of object-oriented classifications depend highly on segmentation results, and while our segmentation was generally good, there were some over- and under-segmented objects. Ultimately, the selection of image segmentation parameters and the complexity of calculating within-object metrics required approximately ten-times longer processing times. Overall, the advantages of object-oriented classification far outweighed its drawbacks. The segments contextualize grey levels within object parameters, and the resulting map has a more generalized appearance than the ‘salt-and-pepper’ pattern in the pixel-based classification. This is attractive for end users because a more generalized view adds to better visual differentiation of land cover types (Dorren et al., 2003; Duro et al., 2012; Stuckens et al., 2000). Interestingly, three studies that compared pixel-based and object-oriented classifications from medium-resolution satellite imagery (Landsat and SPOT) did not find significant differences (Duro et al., 2012; Prudente et al., 2017; Robertson and King, 2011). However, for post-2000 commercial high-resolution imagery, object-oriented classification clearly outperforms pixel-based classification with and without the DEM (Chen and Tian, 2020; Cleve et al., 2008), which is also what we found for classifications of Corona imagery.

Highly heterogeneous mountain areas, such as the Caucasus region (Reinhold et al., 2016), presented a challenging test site for land cover classifications because of reflectance differences introduced by cast shadows in steep terrain, and overall highly variable illumination conditions (Buchner et al., 2020; Chen et al., 2021). Generally, heterogeneous landscapes and land cover transition zones, along with spectrally similar land cover classes tend to result in lower accuracies (Song et al., 2013). We achieved the highest classification accuracy by combining the DEM with our texture metrics. Using only spectral and texture information, our classifications had some confusion between lakes and forests. However, since lakes are flat, the ‘slope’ metric helped differentiate lakes from forests. Confusion between snow-and-ice and urban areas, as well as the barren class were also minimized by adding the DEM. Our results support the findings from other studies that including elevation data when mapping the land cover in mountainous regions can greatly improve land cover classifications (Balzter et al., 2015; Buchner et al., 2020; Chen et al., 2017).

The land cover in our study area in 1964 was diverse. The mountainous areas in Georgia, which were partly covered by snow in our imagery, were heavily forested. Livestock production was historically one of the main sources of food and income in the Caucasus because grasslands were widespread (Hopkins et al., 2012). Croplands dominated the mostly level areas of our study region in southern Russia. Agricultural policies introduced by the Soviet government in the 1960s resulted in rapid agricultural development in many regions of the Soviet Union (Taff et al., 2010), including the Caucasus region (McCauley, 1976). To this date, similar to many Eastern European countries (Feranec et al., 2016), agriculture remains an important component of the economy in the Caucasus (Worden and de Beurs, 2020). As a result, a large variety of crops are grown and there are many large gardens and orchards, which we included in the forest class because of their woody vegetation.

While our overall classification accuracy was high, there were some notable errors and limitations in our datasets. One source of errors was noise and scanning errors in the Corona images (Gheyle et al., 2011). The accuracy of our image orthorectification depended to some extent

on where current high-resolution imagery was available in Google and Bing. Previous studies (e.g., Shortridge and Messina, 2011) found that SRTM error magnitudes are generally larger for sites with higher forest cover and slope, as measured by the standard deviation of error, the RMSE, and the 90% error. The errors rise monotonically with increasing slope and forest cover percent. In our study, the geolocation mismatch between Corona image and SRTM varies from 5.9 to 26.7 m (lower than the size of a SRTM pixel). This can affect the extraction of elevation and slope in highly heterogeneous terrains, due to the rapid changes between neighboring pixels, and therefore the classification of small patches of land cover classes situated in those environments. Fortunately, our study area had slopes steeper than 35° only in 6.8% of the area, and only 0.4% of forested areas occurred in small patches. Furthermore, we gathered our training and validation samples using only visual image interpretation because of the lack of independent data for 1964. However, the high resolution of Corona satellite data allowed in almost all cases to unambiguously identify the land cover for training and validation data (Pengra et al., 2020; Tarko et al., 2020). Lastly, our DEM was derived from satellite data recorded in 2000 and has a spatial resolution of 30 m, which may have affected the classification accuracy. However, the accuracy assessment showed nevertheless a strong improvement when adding the DEM. For further analyses of Corona images, we suggest extracting the high-resolution digital surface model from the Corona data itself whenever full stereoscopic coverage is available is worth considering (Ghuffar et al., 2022). Furthermore, it would be interesting to explore Corona image classifications using convolutional neural networks methods. We opted against them due to their need for very large training datasets, but high-resolution Corona imagery may be well suited for such deep learning approaches. In summary though, despite all of these challenges, our object-oriented land cover mapping with incorporation of the DEM was successful in mapping land cover in a highly heterogeneous and large area.

Given the high accuracy of our final resulting map and the broad availability of historical Corona imagery, we suggest that our approach can facilitate large-area and long-term land use studies in many other regions across the globe. To map areas larger than our study area would require analyzing imagery from multiple Corona paths, and hence different dates and sometimes camera parameters. The extent to which training data signatures from one Corona path could be extended for use in a neighboring path is unclear, but in principle, even larger areas could be mapped. Our approach can advance long-term land use change analyses by combining Corona-based classifications for the 1960s with more recent land cover classifications derived, for example, Landsat or Sentinel-2 imagery. However, due to differences in spatial and spectral resolution, such comparison of Corona data to more recent satellite images would require development and application of customized change detection methods, and just overlaying the different land cover classifications would not be valid.

In conclusion, accurate land cover maps are crucial for land management and global change monitoring, and we demonstrated here that single-date panchromatic Corona satellite imagery can be classified accurately resulting in high-resolution land cover maps for the 1960s. Our results indicate that the object-oriented classification is best, and that including a DEM substantially improves classification accuracy. Our map of broad land cover types in a large and highly heterogeneous area shows the potential of our approach and suggests that similar maps could be made in most landscapes globally, thereby extending the temporal baseline for land use studies to the mid-20th century.

CRedit authorship contribution statement

Afag Rizayeva: Conceptualization, Methodology, Software, Validation, Formal analysis, Investigation, Data curation, Writing – original draft, Visualization. **Mihai D. Nita:** Conceptualization, Methodology, Software, Validation, Formal analysis, Writing – review & editing. **Volker C. Radeloff:** Conceptualization, Methodology, Resources,

Supervision, Project administration, Funding acquisition, Writing – review & editing.

Declaration of Competing Interest

All authors declare that they have no known competing financial interests or personal relationships that could have appeared to influence their work.

Data availability

We have shared the link to our data and codes within the manuscript.

Acknowledgements

We gratefully acknowledge support for this work by the National Aeronautics and Space Administration (NASA) Land-cover and Land-Use Change (LCLUC) Program (Grants 80NSSC18K0316 and 80NSSC18K0343). L. Farwell, K. Lewinska, E. Silveira, H. Yin, N. Kasraee and three anonymous reviewers provided valuable assistance for our analysis, feedback for our results, and constructive comments, which greatly helped improve this manuscript.

Appendix A. Supplementary data

Supplementary data to this article can be found online at <https://doi.org/10.1016/j.rse.2022.113343>.

References

- Achanta, R., Süsstrunk, S., 2017. Superpixels and polygons using simple non-iterative clustering. *IEEE Conf. Comput. Vis. Pattern Recognit.* 4651–4660.
- Agisoft Metashape Professional (Version 1.7.2) (Software), 2021. <http://www.agisoft.com/downloads/installer/>.
- Altmaier, A., Kany, C., 2002. Digital surface model generation from Corona satellite images. *ISPRS J. Photogramm. Remote Sens.* 56, 221–235.
- Andersen, G.L., 2006. How to detect desert trees using corona images: discovering historical ecological data. *J. Arid Environ.* 65, 491–511.
- Balster, H., Cole, B., Thiel, C., Schumliuss, C., 2015. Mapping CORINE land cover from sentinel-1A SAR and SRTM digital elevation model data using random forests. *Remote Sens.* 7, 14876–14898.
- Barichivich, J., Briffa, K.R., Myneni, R.B., Osborn, T.J., Melvin, T.M., Ciais, P., Piao, S., Tucker, C., 2013. Large-scale variations in the vegetation growing season and annual cycle of atmospheric CO₂ at high northern latitudes from 1950 to 2011. *Glob. Chang. Biol.* 19, 3167–3183.
- Beck, A., Philip, G., Abdulkarim, M., Donoghue, D., 2007. Evaluation of Corona and Ikonos high resolution satellite imagery for archaeological prospection in western Syria. *Antiquity* 81, 161–175.
- Blaschke, T., 2010. Object based image analysis for remote sensing. *ISPRS J. Photogramm. Remote Sens.* 65, 2–16.
- Blaschke, T., Lang, S., Lorup, E., Strobl, J., Zeil, P., 2000. Object-oriented image processing in an integrated GIS/remote sensing environment and perspectives for environmental applications. In: Blaschke, T., Lang, S., Lorup, E., Strobl, J., Zeil, P. (Eds.), *Environmental Information for Planning, Politics and the Public*, pp. 555–570.
- Bolch, T., Buchroithner, M., Pieczonka, T., Kunert, A., 2008. Planimetric and volumetric glacier changes in the khumbu himal, Nepal, since 1962 using Corona, Landsat TM and ASTER data. *J. Glaciol.* 54, 592–600.
- Buchner, J., Yin, H., Frantz, D., Kuemmerle, T., Askerov, E., Bakuradze, T., Bleyhl, B., Elizbarashvili, N., Komarova, A., Lewińska, K.E., Rizayeva, A., Sayadyan, H., Tan, B., Tepanosyan, G., Zazanasvili, N., Radeloff, V.C., 2020. Land-cover change in the Caucasus Mountains since 1987 based on the topographic correction of multi-temporal Landsat composites. *Remote Sens. Environ.* 248, 111967.
- Casana, J., Cothren, J., Kalayci, T., 2012. Swords into ploughshares: archaeological applications of Corona satellite imagery in the near east. *Internet Archaeol.* 32.
- Chen, B., Huang, B., Xu, B., 2017. Multi-source remotely sensed data fusion for improving land cover classification. *ISPRS J. Photogramm. Remote Sens.* 124, 27–39.
- Chen, S., Woodcock, C.E., Bullock, E.L., Arévalo, P., Torchinava, P., Peng, S., Olofsson, P., 2021. Monitoring temperate forest degradation on Google Earth Engine using Landsat time series analysis. *Remote Sens. Environ.* 265, 112648.
- Chen, Y., Tian, S., 2020. Comparison of pixel- and object-based image analysis for tea plantation mapping using hyperspectral Gaofen-5 and synthetic aperture radar data. *J. Appl. Remote. Sens.* 14, 044516.
- Cleve, C., Kelly, M., Kearns, F.R., Moritz, M., 2008. Classification of the wildland-urban interface: a comparison of pixel- and object-based classifications using high-resolution aerial photography. *Comput. Environ. Urban. Syst.* 32, 317–326.
- Clinton, N., Holt, A., Scarborough, J., Yan, L.I., Gong, P., 2010. Accuracy assessment measures for object-based image segmentation goodness. *Photogramm. Eng. Remote Sens.* 76, 289–299.
- Conesa, F.C., Madella, M., Galiatsatos, N., Balbo, A.L., Rajesh, S.V., Ajithprasad, P., 2015. Corona photographs in monsoonal semi-arid environments: Addressing archaeological surveys and historical landscape dynamics over North Gujarat, India. *Archaeol. Prospect.* 22, 75–90.
- Connors, R.W., Trivedi, M.M., Harlow, C.A., 1984. Segmentation of a high-resolution urban scene using texture operators. *Comput. Vision Graph. Image Process.* 25, 273–310.
- Crossley, M.S., Burke, K.D., Schoville, S.D., Radeloff, V.C., 2021. Recent collapse of crop belts and declining diversity of US agriculture since 1840. *Glob. Chang. Biol.* 27, 151–164.
- Cui, G., Lv, Z., Li, G., Benediktsson, J.A., Lu, Y., 2018. Refining land cover classification maps based on dual-adaptive majority voting strategy for very high resolution remote sensing images. *Remote Sens.* 10, 1238.
- Deshpande, P., Belwalkar, A., Dikshit, O., Tripathi, S., 2021. Historical land cover classification from CORONA imagery using convolutional neural networks and geometric moments. *Int. J. Remote Sens.* 42, 5148–5175.
- Dittrich, A., Buerkert, A., Brinkmann, K., 2010. Assessment of land use and land cover changes during the last 50 years in oases and surrounding rangelands of Xinjiang, NW China. *J. Agric. Rural. Dev. Trop. Subtrop.* 111, 129–142.
- Dorren, L.K.A., Maier, B., Seijmonsbergen, A.C., 2003. Improved Landsat-based forest mapping in steep mountainous terrain using object-based classification. *For. Ecol. Manag.* 183, 31–46.
- Duro, D.C., Franklin, S.E., Dubé, M.G., 2012. A comparison of pixel-based and object-based image analysis with selected machine learning algorithms for the classification of agricultural landscapes using SPOT-5 HRG imagery. *Remote Sens. Environ.* 118, 259–272.
- Evenson, R.E., Gollin, D., 2003. Assessing the impact of the green revolution, 1960 to 2000. *Science* 300, 758–762.
- Farr, T.G., Rosen, P.A., Caro, E., Crippen, R., Duren, R., Hensley, S., Kobrick, M., Paller, M., Rodriguez, E., Roth, L., Seal, D., Shaffer, S., Shimada, J., Umland, J., Werner, M., Oskin, M., Burbank, D., Alsdorf, D., 2007. The shuttle radar topography mission. *Rev. Geophys.* 45, RG2004.
- Farwell, L.S., Gudex-Cross, D., Anise, I.E., Bosch, M.J., Olah, A.M., Radeloff, V.C., Razenkova, E., Rogova, N., Silveira, E.M.O., Smith, M.M., Pidgeon, A.M., 2021. Satellite image texture captures vegetation heterogeneity and explains patterns of bird richness. *Remote Sens. Environ.* 253, 112175.
- Fekete, A., 2020. CORONA high-resolution satellite and aerial imagery for change detection assessment of natural hazard risk and urban growth in El Alto/La Paz in Bolivia, Santiago de Chile, Yungay in Peru, Qazvin in Iran, and Mount St. Helens in the USA. *Remote Sens.* 12, 3246.
- Feranec, J., Soukup, T., Taff, G.N., Stych, P., Bicik, I., 2016. Overview of changes in land use and land cover in Eastern Europe. In: Gutman, G., Radeloff, V.C. (Eds.), *Land-Cover and Land-Use Changes in Eastern Europe after the Collapse of the Soviet Union in 1991*. Springer International Publishing, Cham, Switzerland, pp. 13–33.
- Foster, D., Swanson, F., Aber, J., Burke, I., Brokaw, N., Tilman, D., Knapp, A., 2003. The importance of land-use legacies to ecology and conservation. *BioScience* 53 (1), 77–88.
- Franklin, S.E., Montgomery, P.K., Stenhouse, G.B., 2005. Interpretation of land cover changes using aerial photography and satellite imagery in the foothills model forest of Alberta. *Can. J. Remote. Sens.* 31, 304–313.
- Galiatsatos, N., Donoghue, D.N.M., Philip, G., 2008. High resolution elevation data derived from stereoscopic Corona imagery with minimal ground control: an approach using Ikonos and SRTM data. *Photogramm. Eng. Remote Sensing* 74, 1093–1106.
- Gheyle, W., Bourgeois, J., Goossens, R., Jacobsen, K., 2011. Scan problems in digital Corona satellite images from USGS archives. *Photogramm. Eng. Remote Sensing* 77, 1257–1264.
- Ghuffar, S., Bolch, T., Rupnik, E., Bhattacharya, A., 2022. A pipeline for automated processing of declassified Corona KH-4 (1962–1972) stereo imagery. *IEEE Trans. Geosci. Remote Sens.* 1.
- Goerlich, F., Bolch, T., Mukherjee, K., Pieczonka, T., Nuth, C., Li, X., Thankabail, P.S., 2017. Glacier mass loss during the 1960s and 1970s in the Ak-Shirak Range (Kyrgyzstan) from Multiple Stereoscopic Corona and Hexagon Imagery, 2017. *Remote Sens.* 9, Page 275 9, 275.
- Gorelick, N., Hancher, M., Dixon, M., Ilyushchenko, S., Thau, D., Moore, R., 2017. Google Earth Engine: planetary-scale geospatial analysis for everyone. *Remote Sens. Environ.* 202, 18–27.
- Gurjar, S.K., Tare, V., 2019. Estimating long-term LULC changes in an agriculture-dominated basin using Corona (1970) and LISS IV (2013–14) satellite images: a case study of Ramganga River, India. *Environ. Monit. Assess.* 191, 217.
- Happ, P.N., Ferreira, R.S., Bentes, C., Costa, G.A.O.P., Feitosa, R.Q., 2010. Multiresolution segmentation: a parallel approach for high resolution image segmentation in multicore architectures. *Int. Arch. Photogramm. Remote. Sens. Spat. Inf. Sci.* 38, C7.
- Haralick, R.M., Dinstein, I., Shanmugam, K., 1973. Textural features for image classification. *IEEE Trans. Syst. Man Cybern.* 3, 610–621.
- Hopkins, A., Rozstalny, A., Airey, J., 2012. Identifying ways to improve competitiveness for small-scale livestock farmers in the countries of Eastern Europe. *Grassl. Sci. Eur.* 17, 747–749.
- Jabs-Sobocińska, Z., Affek, A.N., Ewiak, I., Nita, M.D., 2021. Mapping mature post-agricultural forests in the Polish eastern Carpathians with archival remote sensing data. *Remote Sens.* 13, 2018.

- Kavzoglu, T., 2017. Object-oriented random forest for high resolution land cover mapping using Quickbird-2 imagery. In: *Handbook of Neural Computation*. Academic Press, pp. 607–619.
- Kavzoglu, T., Tonbul, H., 2018. An experimental comparison of multi-resolution segmentation, slic and k-means clustering for object-based classification of vhr imagery. *Int. J. Remote Sens.* 39, 6020–6036.
- Kennedy, D., 1998. Declassified satellite photographs and archaeology in the Middle East: case studies from Turkey. *Antiquity* 72, 553–561.
- Khare, S., Ghosh, S., 2016. Satellite remote sensing technologies for biodiversity monitoring and its conservation. *Int. J. Adv. Earth Sci. Eng.* 5, 375–389.
- Klimetzek, D., Stăncioiu, P.T., Paraschiv, M., Niță, M.D., 2021. Ecological monitoring with spy satellite images—the case of red wood ants in Romania. *Remote Sens.* 13, 520.
- Kressler, F.P., Kim, Y.S., Steinnocher, K.T., 2003. Object-oriented land cover classification of panchromatic KOMPSAT-1 and SPOT-5 data. In: *Proceedings of the International Geoscience and Remote Sensing Symposium (IGARSS)*, pp. 3471–3473.
- Kuhn, M., Johnson, K., 2013. Applied predictive modeling. *Appl. Predict. Model.* 1–600.
- Kusanagi, M., Nogami, J., Chemin, Y., Wandgi, T.J., OO, K.S., Rudrappa, P.B., Van Hieu, D., 2003. Corona declassified imagery for land use mapping: Application to Koh Chang, Thailand. In: *Proceedings of the KRSR Conference*. The Korean Society of Remote Sensing, pp. 891–893.
- Lackner, M., Conway, T.M., 2008. Determining land-use information from land cover through an object-oriented classification of IKONOS imagery. *Can. J. Remote. Sens.* 34, 77–92.
- Lasaponara, R., Yang, R., Chen, F., Li, X., Masini, N., 2018. Corona satellite pictures for archaeological studies: a review and application to the lost Forbidden City of the Han-wei dynasties. *Surv. Geophys.* 39, 1303–1322.
- Li, X., Chen, W.Y., Sanesi, G., Laforzezza, R., 2019. Remote sensing in urban forestry: recent applications and future directions. *Remote Sens.* 11, 1144.
- Li, X., Zhao, S., Rui, Y., Tang, W., 2007. An object-based classification approach for high-spatial resolution imagery. In: Ju, W., Zhao, S. (Eds.), *Geoinformatics 2007: Remotely Sensed Data and Information*. SPIE, p. 675230.
- Lorenz, H., 2004. Integration of Corona and Landsat thematic mapper data for bedrock geological studies in the high Arctic. *Int. J. Remote Sens.* 25, 5143–5162.
- LUCAS, 2022. accessed on 10/03/2022 [WWW Document]. URL (accessed 3.10.22). https://ec.europa.eu/eurostat/statistics-explained/index.php?title=LUCAS_-_Land_use_and_land_cover_survey.
- Ma, L., Li, M., Ma, X., Cheng, L., Du, P., Liu, Y., 2017. A review of supervised object-based land-cover image classification. *ISPRS J. Photogramm. Remote Sens.* 130, 277–293.
- Maxwell, A.E., Shobe, C.M., 2022. Land-surface parameters for spatial predictive mapping and modeling. *Earth-Sci. Rev.* 226, 103944.
- McCauley, M., 1976. Khrushchev and the Development of Soviet Agriculture: Virgin Land Program, 1953–64. Holmes & Meier, New York.
- McMahon, R., 2021. *The Cold War: A Very Short Introduction*, second. ed. Oxford University Press (OUP), Oxford.
- Mészáros, M., Szatmári, J., Tobak, Z., Mucsi, L., 2008. Extraction of digital surface models from Corona satellite stereo images. *J. Env. Geogr.* 1, 5–10.
- Molinario, A.M., Simon, R., Pfeiffer, R.M., 2005. Prediction error estimation: a comparison of resampling methods. *Bioinformatics* 21, 3301–3307.
- Moser, G., Serpico, S.B., Benediktsson, J.A., 2012. Land-cover mapping by markov modeling of spatial-contextual information in very-high-resolution remote sensing images. *Proc. IEEE* 101, 631–651.
- Munteanu, C., Kamp, J., Nita, M.D., Klein, N., Kraemer, B.M., Müller, D., Koshkina, A., Prishchepov, A.V., Kuemmerle, T., 2020. Cold war spy satellite images reveal long-term declines of a philopatric keystone species in response to cropland expansion. *Proc. R. Soc. B Biol. Sci.* 287, 20192897.
- Munteanu, C., Kuemmerle, T., Boltziar, M., Lieskovský, J., Mojses, M., Kaim, D., Konkoly-Gyuró, É., Mackovčin, P., Müller, D., Ostapowicz, K., Radeloff, V.C., 2017. Nineteenth-century land-use legacies affect contemporary land abandonment in the Carpathians. *Reg. Environ. Chang.* 17, 2209–2222.
- Munteanu, C., Senf, C., Nita, M.D., Sabatini, F.M., Oeser, J., Seidl, R., Kuemmerle, T., 2021. Leveraging historical spy satellite photographs and recent remote sensing data to identify high conservation value forests. *Conserv. Biol.* 36, e13820.
- Myers, N., Mittermeier, R.A., Mittermeier, C.G., Da Fonseca, G.A.B., Kent, J., 2000. Biodiversity hotspots for conservation priorities. *Nature* 403, 853–858.
- Nghi, D.H., Mai, L.C., 2008. An object-oriented classification techniques for high resolution satellite imagery. In: *Proceedings of the International Symposium on Geoinformatics for Spatial Infrastructure Development in Earth and Allied Sciences (GIS-IDEAS)*, pp. 230–240.
- Nita, M.D., Munteanu, C., Gutman, G., Abrudan, I.V., Radeloff, V.C., 2018. Widespread forest cutting in the aftermath of world war II captured by broad-scale historical Corona spy satellite photography. *Remote Sens. Environ.* 204, 322–332.
- Norris, P., 2007. *Spies in the Sky: Surveillance Satellites in War and Peace*. Springer-Praxis, Chichester.
- NRO, 1967. Description and operation manual: J-3 panoramic camera system. In: *National Reconnaissance Office Data Book*. Itek Corporation, Lexington.
- Olofsson, P., Foody, G.M., Herold, M., Stehman, S.V., Woodcock, C.E., Wulder, M.A., 2014. Good practices for estimating area and assessing accuracy of land change. *Remote Sens. Environ.* 148, 42–57.
- Peebles, C., 1997. *The Corona Project: America's First Spy Satellites*. Naval Inst Press, Annapolis.
- Pengra, B.W., Stehman, S.V., Horton, J.A., Dockter, D.J., Schroeder, T.A., Yang, Z., Cohen, W.B., Healey, S.P., Loveland, T.R., 2020. Quality control and assessment of interpreter consistency of annual land cover reference data in an operational national monitoring program. *Remote Sens. Environ.* 238, 111261.
- Picard, R.R., Cook, R.D., 1984. Cross-validation of regression models. *J. Am. Stat. Assoc.* 79, 575–583.
- Prudente, V.H.R., da Silva, B.B., Johann, J.A., Mercante, E., Oldoni, L.V., 2017. Comparative assessment between per-pixel and object-oriented for mapping land cover and use. *Eng. Agrícola* 37, 1015–1027.
- R Core Team, 2022. R: A language and environment for statistical computing (Version 4.1.1). <https://www.R-project.org/>.
- Reinhold, S., Belinskiy, A., Korobov, D., 2016. Caucasia top-down: remote sensing data for survey in a high altitude mountain landscape. *Quat. Int.* 402, 46–60.
- Rendenieks, Z., Nita, M.D., Nikodemus, O., Radeloff, V.C., 2020. Half a century of forest cover change along the Latvian-Russian border captured by object-based image analysis of Corona and Landsat TM/OLI data. *Remote Sens. Environ.* 249, 112010.
- Rigina, O., 2003. Detection of boreal forest decline with high-resolution panchromatic satellite imagery. *Int. J. Remote Sens.* 24, 1895–1912.
- Robertson, L.D., King, D.J., 2011. Comparison of pixel- and object-based classification in land cover change mapping. *Int. J. Remote Sens.* 32, 1505–1529.
- Robinson, C., Hou, L., Malkin, K., Soobitsky, R., Czawlytko, J., Jojic, N., 2019. Large scale high-resolution land cover mapping with multi-resolution data. In: *Proceedings of the IEEE/CVF Conference on Computer Vision and Pattern Recognition*, pp. 12726–12735.
- Ruelland, D., Tribotte, A., Puech, C., Dieulin, C., 2011. Comparison of methods for LUCC monitoring over 50 years from aerial photographs and satellite images in a Sahelian catchment. *Int. J. Remote Sens.* 32, 1747–1777.
- Ruiz Hernandez, I.E., Shi, W., 2017. A Random Forests classification method for urban land-use mapping integrating spatial metrics and texture analysis. <https://doi.org/10.1080/01431161.2017.1395968> 39, 1175–1198.
- Saleem, A., Corner, R., Awange, J., 2018. On the possibility of using Corona and Landsat data for evaluating and mapping long-term LULC: case study of Iraqi Kurdistan. *Appl. Geogr.* 90, 145–154.
- Shahtamassebi, A.R., Lin, Y., Lin, L., Atkinson, P.M., Moore, N., Wang, K., He, S., Huang, L., Wu, J., Shen, Z., Gan, M., Zheng, X., Su, Y., Teng, H., Li, X., Deng, J., Sun, Y., Zhao, M., 2017. Reconstructing historical land cover type and complexity by synergistic use of landsat multispectral scanner and Corona. *Remote Sens.* 9, 682.
- Shortridge, A., Messina, J., 2011. Spatial structure and landscape associations of SRTM error. *Remote Sens. Environ.* 115, 1576–1587.
- Song, D.X., Huang, C., He, T., Feng, M., Li, A., Li, S., Pang, Y., Wu, H., Mohamed Shariff, A.R., Townshend, J., 2021. Very rapid forest cover change in Sichuan Province, China: 40 years of change using images from declassified spy satellites and Landsat. *IEEE J.Sel. Top. Appl. Earth Obs. Remote Sens.* 14, 10964–10976.
- Song, D.X., Huang, C., Sexton, J.O., Channan, S., Feng, M., Townshend, J.R., 2015. Use of landsat and Corona data for mapping forest cover change from the mid-1960s to 2000s: case studies from the eastern United States and Central Brazil. *ISPRS J. Photogramm. Remote Sens.* 103, 81–92.
- Song, X.-P., Huang, C., Feng, M., Sexton, J.O., Channan, S., Townshend, J.R., 2013. Integrating global land cover products for improved forest cover characterization: an application in North America. *Int. J. Digit. Earth* 7, 709–724.
- Song, X.P., Huang, C., Townshend, J.R., 2017. In: *Improving global land cover characterization through data fusion*, 20, pp. 141–150. <http://www.tandfonline.com/action/journalInformation?show=aimsScope&journalCode=tsi20#>. Vs XpLiCLRHE.
- Stăncioiu, P.T., Niță, M.D., Fedorca, M., 2021. Capercailie (Tetrao urogallus) habitat in Romania – a landscape perspective revealed by cold war spy satellite images. *Sci. Total Environ.* 781, 146763.
- Stratoulas, D., Kabadayi, M., 2020. Land cover feature extraction from Corona spy satellite images during the Cold War-1968. In: *Proceedings of the IGARSS 2020 – 2020 IEEE International Geoscience and Remote Sensing Symposium*, pp. 6069–6072.
- Stuckens, J., Coppin, P.R., Bauer, M.E., 2000. Integrating contextual information with per-pixel classification for improved land cover classification. *Remote Sens. Environ.* 71, 282–296.
- Taff, G.N., Müller, D., Kuemmerle, T., Ozdenler, E., Walsh, S.J., 2010. Reforestation in central and Eastern Europe after the breakdown of socialism. In: Nagendra, H., Southworth, J. (Eds.), *Reforesting Landscapes: Linking Pattern and Process*. Springer Landscape Series, Dordrecht, New York, pp. 121–147.
- Tappan, G.G., Hadj, A., Wood, E.C., Lietzow, R.W., 2000. Use of Argon, Corona, and landsat imagery to assess 30 years of land resource changes in west-Central Senegal. *Photogramm. Eng. Remote Sensing* 66, 727–735.
- Tarko, A., Tsendbazar, N.E., de Bruin, S., Bregt, A.K., 2020. Producing consistent visually interpreted land cover reference data: learning from feedback. <https://doi.org/10.1080/17538947.2020.1729878> 14, 52–70.
- Ullman, S., 1979. The interpretation of structure from motion. *Proc. R. Soc. Lond. B Biol. Sci.* 203, 405–426.
- United Nations, 2019. World population prospects: The 2019 revision. Department of Economic and Social Affairs, Population Division, New York, NY.
- USGS, 2019. image courtesy of U.S. Geological Survey [WWW Document]. URL <https://earthexplorer.usgs.gov/>.
- Veroustraele, F., Fang, H., Xi, C., Bao, A.M., Dong, Q., Tie, L., Willems, P., 2011. Diachronic mapping of LUCC in the northwest of China over the last half century: conversion of Corona panchromatic reflectance into landsat NDVI imagery. *Insinciences J.* 1, 194–210.
- Wardlow, B.D., Egbert, S.L., 2003. A state-level comparative analysis of the GAP and NLCD land-cover data sets. *Photogramm. Eng. Remote Sensing* 69, 1387–1397.
- White, M.A., de Beurs, K.M., Didan, K., Inouye, D.W., Richardson, A.D., Jensen, O.P., O'Keefe, J., Zhang, G., Nemani, R.R., van Leeuwen, W.J.D., Brown, J.F., de Wit, A., Schaepman, M., Lin, X., Dettinger, M., Bailey, A.S., Kimball, J., Schwartz, M.D., Baldocchi, D.D., Lee, J.T., Lauenroth, W.K., 2009. Intercomparison, interpretation,

- and assessment of spring phenology in North America estimated from remote sensing for 1982–2006. *Glob. Chang. Biol.* 15, 2335–2359.
- Worden, J., de Beurs, K.M., 2020. Surface water detection in the Caucasus. *Int. J. Appl. Earth Obs. Geoinf.* 91, 102159.
- Wu, J., Feng, Z., Gao, Y., Peng, J., 2013. Hotspot and relationship identification in multiple landscape services: a case study on an area with intensive human activities. *Ecol. Indic.* 29, 529–537.
- Yin, H., Brandão, A., Buchner, J., Helmers, D., Iuliano, B.G., Kimambo, N.E., Lewińska, K. E., Razenkova, E., Rizayeva, A., Rogova, N., Spawn, S.A., Xie, Y.H., Radeloff, V.C., 2020. Monitoring cropland abandonment with Landsat time series. *Remote Sens. Environ.* 246, 111873.
- Zazanashvili, N., Mallon, D., 2009. Status and protection of globally threatened species in the Caucasus, CEPF. WWF, Contour Ltd, Tbilisi.
- Zhang, H., Fritts, J.E., Goldman, S.A., 2008. Image segmentation evaluation: a survey of unsupervised methods. *Comput. Vis. Image Underst.* 110, 260–280.
- Zhang, Y., Shen, W., Li, M., Lv, Y., 2020. Integrating landsat time series observations and Corona images to characterize forest change patterns in a mining region of Nanjing, eastern China from 1967 to 2019. *Remote Sens.* 12, 1–21.
- Zheng, L., Wan, L., Huo, H., Fang, T., 2014. A noise removal approach for object-based classification of VHR imagery via post-classification. In: *Proc. IEEE Int. Conf. Audio, Lang. Image Process*, pp. 915–920.
- Zhu, Z., Woodcock, C.E., 2014. Continuous change detection and classification of land cover using all available Landsat data. *Remote Sens. Environ.* 144, 152–171.